



Exploring various Integration Methods of carbon quantum dots in CsPbCl₃ perovskite solar cells for enhanced power conversion efficiency

Eman F. Sawires¹, Zahraa Ismail², Mona Samir³, Ahmed M. Agour^{3,4}, Fathy Z. Amer¹, Hassan Nageh³, and Sameh O. Abdellatif^{2,5,*} 

¹ The Electronics and Communications Engineering Department, Faculty of Engineering, Helwan University, Cairo, Egypt

² The Electrical Engineering department and FabLab, Centre for Emerging Learning Technologies CELT, British University in Egypt (BUE), Cairo 11387, Egypt

³ The Nanotechnology Research Centre (NTRC), The British University in Egypt, Cairo 11387, Egypt

⁴ The School of Science and Engineering, The American University in Cairo, New Cairo 11835, Egypt

⁵ The British University in Egypt, Misr Ismailia Desert Road, PO Box 43, El-Sherouk City 11387, Egypt

Received: 6 March 2024

Accepted: 24 March 2024

Published online:

18 April 2024

© The Author(s), 2024

ABSTRACT

In this study, we explore the integration of carbon quantum dots (QDs) in cesium lead halide perovskite solar cells (PSCs) across the electron transport layer (ETL), hole transport layer (HTL), and the perovskite absorber to enhance power conversion efficiency (PCE). We conduct a comprehensive investigation from thin film analysis to complete device characterization, encompassing eight different device topologies. Our results reveal that the integration of QDs in various layers significantly impacts the performance of the PSCs. Notably, adding QDs in the HTL and ETL improves charge transport and reduces recombination, enhancing device efficiency. Furthermore, introducing QDs in the perovskite layer leads to modifications in the energy landscape, reducing charge trapping and enhancing stability. We observe a trade-off between short-circuit current and overall PCE, with different QD integration strategies yielding distinct performance outcomes. Additionally, incorporating QDs in the ETL layer reduces hysteresis, attributed to mitigated ion migration and charge-trapping effects. Overall, the addition of QDs in these layers demonstrates improved charge transport, reduced recombination, and enhanced stability, ultimately contributing to the enhanced performance and efficiency of perovskite solar cells, reaching 22.5%. This study paves the way for future investigations into the potential of QDs in PSC technology and their impact on device forecasting and operational stability.

Address correspondence to E-mail: Sameh.osama@bue.edu.eg

1 Introduction

Perovskites are hybrid compounds made from organic components and metal halides [1–5]. They have great potential in many applications, e.g., photodetectors [6], lasers [7], transistors [8], and LED lights [9], but their primary influence lies in solar cells, where they are poised to surpass the market of similar products silicon [1, 10–15]. One of the difficulties facing the commercialization of perovskite solar cells (PSCs) is that their operational stability drops as they scale up and power conversion efficiency (PCE), making it a challenge to maintain high performance in a complete PSC [16]. There are severe hysteresis effects and a mismatch in the energy level alignment within the PSCs, which are unfavorable for the photovoltaic properties of devices and charge transport [17]. The problems are partly with the solar cell's electron transport layer (ETL), hole transport layer (HTL), and perovskite absorbing layer [17–20].

Some methods have been proposed for improving the performance of PSCs involving passivating surface defects of the perovskite layer [21]. The passivated surface generates fewer carrier recombination centers, accordingly enhancing the contact interfaces between the carrier transport layer and the perovskite layer [22]. Alternatively, modifying the composition of the perovskite (ABX_3), involving a combination of other auxiliary ions in the entire structure, or replacing the A-cation with Cesium ions, B-cation by Mn ions, and the X-anion by a combination of halogen ions [23] and in addition, changing interfacial contact environments by presenting an additional interface layer [18, 24]. This extra layer can enhance the alignment of the energy level of the corresponding layers. Sensible arrangement of energy levels helps the extraction of carriers. Accordingly, it leads to an improvement in stability, lowering the contact resistance and decreasing the carrier recombination ratios [18] and developing and optimizing the hole transport layer and electron transport layer [18, 20]. With an enhanced conductivity of HTL or ETL in devices or a suitable HOMO/LUMO level, their performance could be efficiently upgraded.

Quantum dots (QDs) are an effective and easy tool used as dopants, interfacial modification materials, charge transport materials, and luminescent downshifting materials [25]. With sizes ranging from 2 to 20 nanometers, QDs, also known as semiconductor nanocrystals (NCs), are synthetic nanoparticles of a

semiconducting substance [26]. Since QDs are predictably combined to be only tens of atoms in diameter, they can constrain electrons to quantized energy levels dependent on the size and shape of the QD. They allow tunable bandgap nanoscale semiconductors controlled by the number of atoms composing the quantum dot—increasing the quantum dot's radius reduces the adequate band gap energy and implies a redshifted color output [25].

It is a unique property of tunable bandgap as a function of shape and size that has motivated precise significance in quantum dots for various technologies [27]. They exhibit unique electronic and optical properties over their bulk counterparts due to efficient and tunable photoluminescence (PL), high color purity, photochemical stability, narrow emission, and unique quantum effects at the atomic level. Moreover, when illuminated, they emit light of specific wavelengths (colors) [27]. The surface functional group and the size usually designate the properties of QDs. Thus, it is likely to prepare a required QD by monitoring the preparation process [28]. They are mainly prepared by low-temperature and thermal injection solution methods. Consequently, QDs are believed to be favorable materials for optimizing PSCs [29]. Therefore, their exclusive optical properties make them ultimate for being incorporated as active elements in a wide variety of optical applications and devices involving photovoltaic devices, biomarkers, lasers, detectors, and light-emitting diodes (LEDs) in the past few decades [28].

Nowadays, many surveys have proved that QDs can be very auspicious candidates for achieving the goals mentioned above of improving the performance of PSCs [30–35]. QDs, materials with exceptional photovoltaic effects and properties, have tunable energy bands, accelerate and enhance the transport of holes and electrons, and optimize the energy level arrangement within PSCs [36]. Moreover, they can also passivate defects on the surface of perovskite films and increase the crystallinity of perovskite films during their crystallization, thus enhancing the film's quality [2, 4, 37].

In this study, we investigate the integration of the QDs in perovskite solar cells, mainly cesium lead halide PSCs, through the three main layers: ETL, HTL, and the perovskite absorber. The investigation is scaled up to device I-V characterization from the thin film, segmented SCs, and physiochemical, optical, and electrical characterization. Thin film-wise, we

compare the thin film performance with and without QDs using SEM, XRD, FTIR, UV-Vis. spectrometer, and morphological surface resistance. The complete devices involve eight different topologies, cf. Fig. 1 demonstrates all possible alternatives for embedding QDs in our PSCs.

2 Experimental work and measurement setups

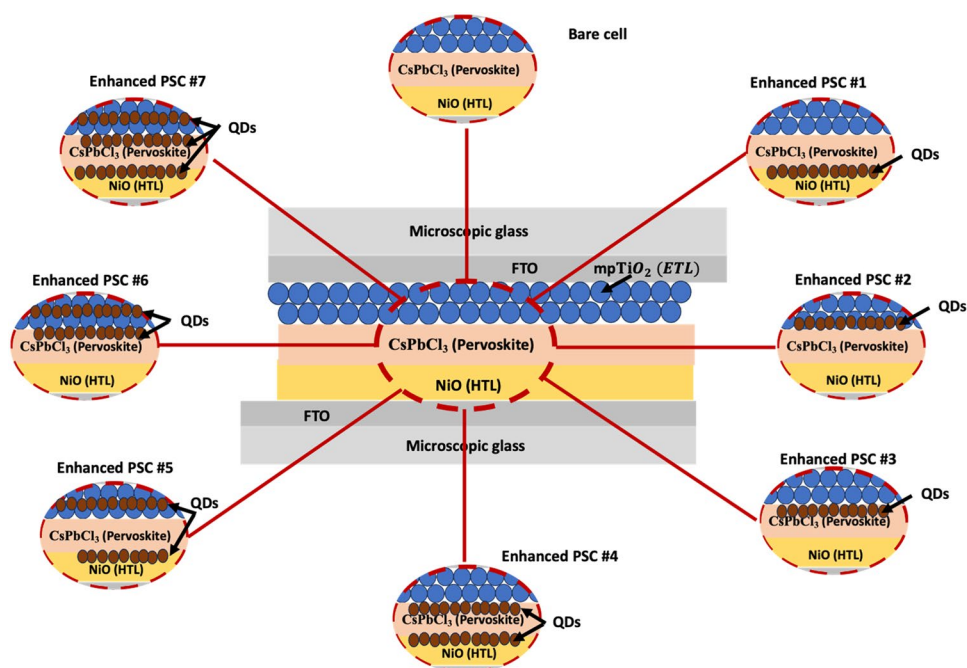
Following the topologies introduced in Fig. 1, we studied the integration possibilities of carbon quantum dots in cesium lead chloride. Our bare cesium lead chloride cell, in Fig. 1, involves NiO's hole transport layer and mesoporous TiO_2 as the electron transport layer [38]. All cells are symmetric with FTO-coated glass as in our previous work in [10, 12, 39, 40]. To prepare NiO nanoparticles, 100 mL of ethanol was used to dissolve 9.9 g of nickel acetate tetrahydrate precursor. Afterward, monoethanolamine (MEA) was directly added, and then a green-colored homogeneous solution was obtained by forceful stirring at 70 °C for almost 4 h.

The CsPbCl_3 layer was created by successive deposition in two steps. First, 367 mg of PbCl_2 were mixed in 0.5 ml DMF and 0.5 ml DMSO for 10 min at 75 °C on a hot plate within a covered container. Subsequently,

2 ml of methanol was used to dissolve 30 mg of CsCl, and the mixture was heated for 10 min in a sealed container. The substrate was then filtered via a 0.22 μm pore size PTFE filter, making it ready for usage. The PbCl_2 layer was spin-coated for 20 s at 500 rpm and then for 30 s at 2000 rpm. After that, it was dried on a hot plate for 30 min at 180 °C. After drying, the substrate was dipped for five to fifteen minutes in a hot solution containing 15 mg/ml CsCl. After that, it was directly heated on a hot plate for 30 min at 180 °C. The TiO_2 layer is deposited using an automatically controlled screen-printing setup with a glass rod [11, 38, 41, 42].

A practical and simple technique has been developed for creating N-doped carbon quantum dots [43], including a hydrothermal synthesis method without any organic solvents, NaOH, or water. 3 g of citric acid and 6 g of urea are used in the synthesis procedure as the foundations of carbon and nitrogen, respectively. 40 ml of deionized water was mixed with the precursors and stirred slightly for 1 h. Afterward, the subsequent mixture is transported to a stainless-steel Teflon container and then exposed to thermal treatment at 160 °C for 3 h, producing a dark greenish colloidal solution of N-doped CQDs. Subsequently, the suspension is centrifuged at 12,000 rpm to remove the large particles, while the residual solution is wisely cleaned with ethanol five times to remove the

Fig. 1 The eight different PSCs investigated in this study with an active area of 25.5 mm²



unreacted precursors. This procedure is considered a cost-effective and environmentally friendly method.

To prepare NiO with N-doped QCs, 1.5 mg of N-doped CQDs was added to 5 mL of NiO precursor solution and stirred at 85 °C and 500 rpm for 2 to 3 h. The color of the resultant solution turns darkish and blackish-green. The TiO₂ layer with N-CQs was already investigated in our previous in [43]. We use a magnetic stirrer to mix 1 gram of titanium dioxide with 40 ml of distilled water. Next, we add CQDs at the desired concentration (30 mg for 3% and 10 mg for 1%). Using a hydrothermal process, we add all the material-containing solution to a Teflon tube, carefully shut it, and bake it for four hours at 120 °C. Following the preceding stage, the material is purified using a centrifuge filled with water and then dried at 70 °C. 3.75 ml of isopropanol should be added to 2.5 gm of TiO₂ or any of the composites (1% or 3%) in 3 ml of triton-X polymer. Following preparation, we apply the composite to the glass's surface and let it dry in the oven for the entire night at 70 degrees.

The mixture of CsPbCl₃ and QDs uses a two-step sequential deposition method as follows: First, 300 mg of CsCl was dissolved in 20 ml of methanol, and then the precursor solution was heated in a sealed container for 15 min at 75 °C. Accordingly, 3670 mg of PbCl₂ and 3 mg of N-doped CQDs were dissolved in 5 mL of DMF and 5 mL of DMSO and then stirred on a hot plate for 3 to 4 h at 75 °C until the color of the solution turned dark black. Afterward, it was filtered by using a 0.22 μm pore size PTFE filter.

For device integration, the FTO-coated glass substrates are washed by sonicating in acetone, isopropanol, and warm deionized water for 25 consecutive minutes. Afterward, they were dried under nitrogen flow in the atmosphere and then treated with UV-ozone cleaner for 20 min. Subsequently, the substrates were annealed at 75 °C before they were used. Afterward, the mesoporous TiO₂, which acts as the ETL, is deposited over the counter electrode by screen printing, followed by a spin-coated layer of CsPbCl₃. On the other hand, the NiO, which acts as the HTL, is then coated over the perovskite layer using a spin coater. Lastly, this electrode is sandwiched with another working electrode with the help of a selling machine. As highlighted in Fig. 1, eight topologies are discussed, considering all possible combinations of QDs, as listed in Table 1.

Scanning electron microscopy (SEM) was used to characterize the micromorphology of the films. An

Table 1 The eight different PSCs investigated in this study with an active area of 25.5 mm²

	Adding QDs to		
	HTL	ETL	Perovskite
Bare Cell			
PSC #1	√		
PSC #2		√	
PSC #3			√
PSC #4	√		√
PSC #5	√	√	
PSC #6		√	√
PSC #7	√	√	√

X-ray diffraction system (XRD) was used to investigate the crystallinity of perovskite films. A UV–Vis spectrophotometer was used to gather UV–Vis-absorption spectra. An infrared spectrometer was used to record FTIR spectra. The surface resistance is explored using our four-probe station. A Keithley 2400 source/meter (Keithley Instruments Inc.) was used to measure the current-voltage characteristics under AM 1.5G simulated sunlight (100 mW cm⁻²), as previously validated in [1].

3 Results and discussion

This section demonstrates the results excluded from this study. The results section is divided into four sub-sections, starting with the thin film morphological and optoelectronic behavior for porous TiO₂, NiO, and CsPbCl₃. Then, the device *I* – *V* characterization is introduced for the eight proposed topologies.

3.1 Mesoporous TiO₂ thin film characteristics

Mesoporous TiO₂ is considered a potential electron transport layer in a wide range of solar cells, including perovskite solar cells [11, 38, 41]. While referring to our previous studies [42, 43], the XRD, FTIR, and optical characterization for both TiO₂ and TiO₂ with carbon-doped quantum dots are well investigated. In this study, we intend to describe the electron transport capabilities of the mp-TiO₂ layer by scanning the morphological surface resistance of thin films of TiO₂ on microscopic glass, with and without quantum dots. The surface resistance of a thin film semiconductor can

provide some insights into carrier transport properties, but it is not a direct indicator of carrier mobility. Surface resistance primarily reflects the resistance to the flow of electrical current across the material's surface. Carrier mobility, on the other hand, is a measure of how quickly charge carriers can move through the material when subjected to an electric field. While surface resistance and carrier mobility are related in the context of charge transport, other factors such as carrier concentration, scattering mechanisms, and the specific crystal structure of the semiconductor also influence carrier mobility.

Using our scanning four-probe station, the thin films of with and with QDs are measured as in Fig. 2. A reduced surface resistance within the ETL indicates an improved electron-transport property. Lower surface resistance facilitates more efficient extraction and transport of electrons from the perovskite layer to the electron transport layer, reducing electron recombination and improving charge collection efficiency. Moreover, lower surface resistance minimizes resistive losses within the ETL, leading to a more efficient flow of electrons towards the electrode. This can help maintain a higher open-circuit voltage and reduce energy losses associated with resistive effects, ultimately contributing to improved PCE, as discussed in section four.

Fig. 2 Morphocail surface resistance for a thin film of **a** mp-TiO₂ and **b** mp-TiO₂/QDs

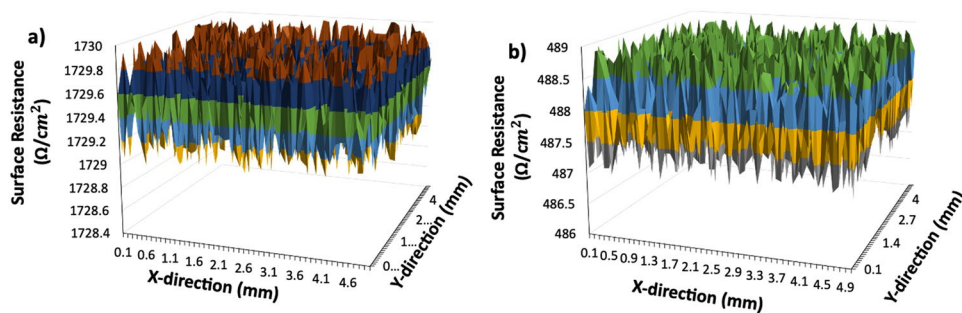
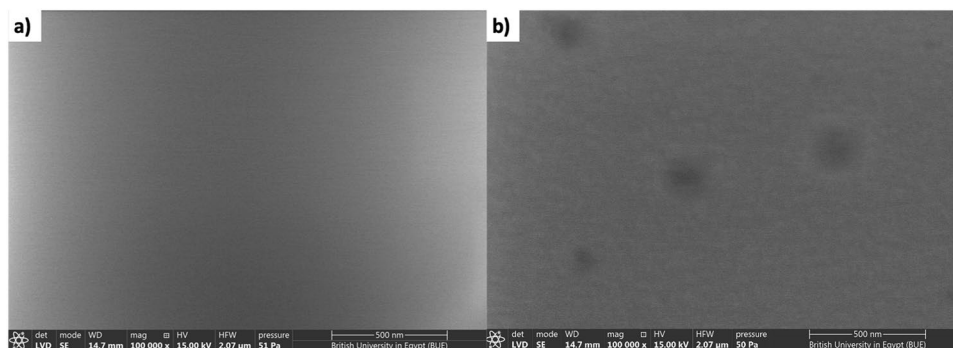


Fig. 3 SEM for a thin film of **a** NiO and **b** NiO//QDs



3.2 NiO thin film characteristics

Following the recipe in Sect. 2, thin films of NiO with and without carbon QDs are prepared on a microscopic glass substrate. To observe the morphological changes and the surface morphological composition of the synthesized sample nanoparticles, SEM analysis was carried out and examined. Figure 3 displays the SEM micrographs of all the synthesized NiO nanoparticles with QDs and without QDs. The findings show that highly crystalline and monodisperse NiO nanoparticles are produced. NiO nanoparticles are uniformly dispersed across the surface, appearing as tiny white particles. We find that NiO with QDs have non-uniform surface structures.

On the other hand, the surface morphology was improved by the grain growth and benzene-shaped nanostructure of the surface obtained with QDs. Nanoclusters are forming as the inertia of the nanofillers to form agglomerations increases with the amount of nanofiller in the nanocomposites. Nanoparticles clump together between adjacent particles due to the attractive van der Waals force. The quantity and size of the nanoparticles within the polymer matrix determine the size of the nanoclusters. NiO film deposited with QDs morphology that is randomly oriented and has more prominent grains. Certain particles appear as

spheres, while others take the form of rods. The particles are densely packed together, resembling a cluster of nanoparticles.

Fourier transform infrared (FTIR) is one of the most crucial measurements to confirm the presence of bonds between the atomic components of NiO NPs with QDs and without QDs. It releases essential information about functional groups' matrix structures and vibrational frequencies. The recorded FTIR spectrum in the range of 4000 cm^{-1} to 400 cm^{-1} is displayed in Fig. 4. It displays the prior and final states following the addition of QDs to the NiO. The CH and CH₂ groups exhibit symmetric and asymmetric stretching vibrations at 2920 and 2844 cm^{-1} , respectively. Peaks at 1000 cm^{-1} were associated with the stretching vibration value for C–N, while 1427 cm^{-1} were correlated with the C–H bending vibration originating from the methylene group. The O=C=O symmetric and asymmetric stretching vibrations and the C–O stretching vibration are responsible for the serrated absorption bands in the 1000 – 1250 cm^{-1} region [44]. The FTIR spectra exhibit C–N stretching at wavenumber 1077 cm^{-1} , suggesting the presence of alkaloids. The stretching vibration of the C=C in an aromatic ring is connected to the band at 1492 cm^{-1} . The peak at 408 cm^{-1} was associated with Ni–O and 835 cm^{-1} with vibrations that emerged in the C–C ring. Ni–O's stretch vibration is the source of the strong vibration band that can be seen at 659 cm^{-1} and 433 cm^{-1} [44, 45]. Following calcination, a strong band at 425 cm^{-1} is visible

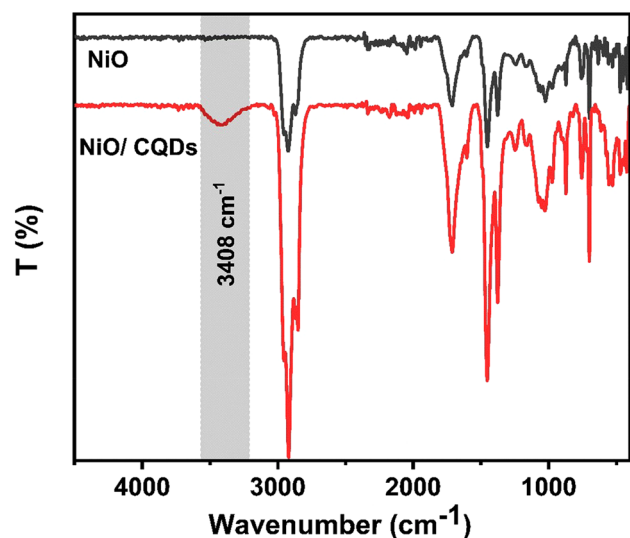


Fig. 4 FTIR for a thin film of NiO and NiO//QDs

in the NiO nanoparticles' FTIR spectra, indicating the Ni–O bond's vibration.

Following the doping of QDs with NiO NPs, new broadband at 3400 – 3700 cm^{-1} appeared at 3408 cm^{-1} , attributed to the spinel structure of N–H, hydrogen vibration O–H, and H₂O molecules bending mode. It indicates the chemically bonded hydroxyl group's stretching vibration mode, typically linked to phenols and carboxylic acids. It is ascribed to the water absorbed on the samples' exterior surface. It was discovered that the value of these bands' intensity increased after the addition of QDs during the calcination process, indicating that the ultrafine powers did not absorb H₂O and CO₂ intensely physically. FTIR analysis of the produced nanocomposites revealed the presence of QDs and NiO nanoparticles, indicating a successful complexation between them.

XRD was used to analyze the phase purity, structure, and crystalline structural parameters of the prepared NiO nanoparticles. Using chemical precipitation to create synthetic NiO nanoparticles, the powder's diffraction pattern was observed at different diffraction angles (2θ) at 10° and 60° . Powder X-ray diffraction (XRD) was used to determine the crystalline parameters of the prepared NiO nanoparticle sample. The product's XRD patterns verify that nickel oxide is the material that was formed. XRD patterns show that the small size effect is responsible for the low and broad diffraction peaks. The X-ray diffraction pattern of the NiO with and without QDs is displayed in Fig. 5.

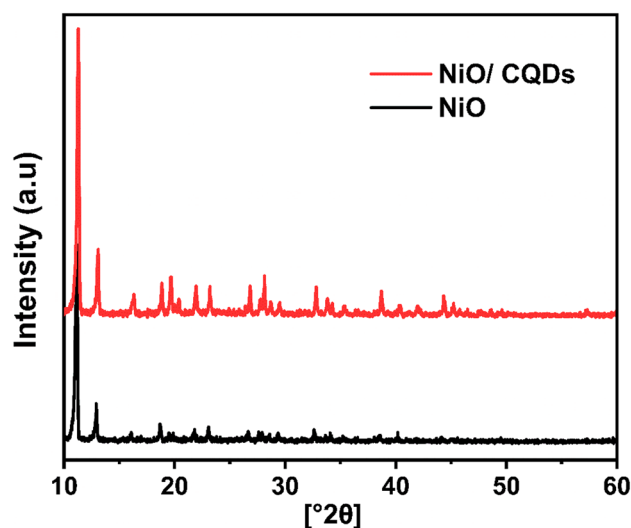


Fig. 5 XRD for a thin film of NiO and NiO//QDs

As for the NiO without QDs, the peaks at 2θ values 11° , 13.85° , 17° , 19.71° , 22.08° , 23.09° , 27.92° , 28.78° , 28.99° , 33.68° , 34.43° , 35.13° , and 40.17° are assigned the miller indices (003), (020), (110), (200), (211), (130), (110), (220), (131), (311), (222), (231,241), and (200). The orientation of the nanoparticles is primarily along the (110) plane. The face-centered cubic phase formation of NiO NPs is suggested by all the visible diffraction peaks at 2θ values. Based on the XRD pattern, the lattice parameter and interplanar spacing are $a = b = c = 4.227 \text{ \AA}$ and $d = 2.114 \text{ \AA}$, respectively, corresponding to the most dominant peak (110). The small size of the particles is evident in Fig. 5, where the diffraction peaks are markedly broadened. $\text{Ni(OH)}_2 \cdot 6\text{H}_2\text{O}$ was the source of the broad diffraction peaks. Their micro-structural distortion or small grain size could cause their broadening. The minuscule particle-like structure may cause some notable broadening of diffraction peaks in Ni(OH)_2 XRD patterns under current experimental conditions. The “sawtooth” reflections in the XRD pattern were typical of two-dimensional turbostratic phases with disordered layers in orientation [44, 45].

As for the NiO NPs with QDs, the sample displayed a crystalline pattern, and all the diffraction peaks at approximately $2\theta = 11^\circ$, 13.85° , 17° , 19.71° , 20.22° , 22.08° , 23.09° , 27.92° , 28.78° , 28.99° , 33.68° , 34.43° , 35.13° , 40.17° , 41.87° , 44.28° , 45.10° , 48.17° , 49.21° , and 49.8° can be well indexed as face-centered cubic phases, which can be ideally related to the (003), (020), (110), (200), (211), (130), (110), (220), (131), (311), (222), (231,241), (200), and (200) crystal planes, respectively, based on the standard nickel oxide pattern. X-ray diffraction patterns show that the powders are present in the purest form, aligned in a single phase, and do not exhibit any significant diffraction peaks other than the usual peaks caused by the FCC phase NiO nanoparticles. Therefore, NiO nanoparticles produced by the physical stages of preparation result in exceptionally pure materials.

The NiO nanoparticles are single-phase, as indicated by the XRD pattern. The Debye-Scherrer formula was used to determine the average nanocrystalline size (D) [46]:

$$D = \frac{0.9\lambda}{\beta \cos\theta} \quad (1)$$

where θ is the Bragg diffraction angle, λ is the X-ray wavelength, and β is the entire width of the diffraction

line at half of the maximum intensity of the XRD peak appearing at the diffraction angle θ . It was discovered that the average crystallite size of NiO NPs was close to 18 nm. The lattice strain also causes the material's XRD pattern to broaden the diffraction peaks.

One of the essential techniques for the optical characteristics of nanoparticles is UV-visible absorption spectroscopy. The literature currently in publication provides extensive documentation on the increased trend of band gap energy about decreases in particle size. Furthermore, it is widely known that quantum confinement effects cause semiconductors with nanoscale size to exhibit a blue shift in their spectra. An increase in the band gap value coincident with the blue shift phenomenon is proof positive of a quantum confinement effect. This suggests that as particle size decreased, the band gap value increased. Because of the photogenerated electron-hole carriers' quantum confinement, the wavelength of the maximum exciton absorption (λ_{max}) generally decreases as particle size decreases.

The variation of the NiO nanoparticles' optical absorbance with wavelength is depicted in Fig. 6. The wavelength range of 300–800 nm has been used to calculate the optical absorption coefficient. In the visible region, the absorption coefficient increased quickly, but at very low photon energies, it was much lower in the UV region. The photogenerated electron-hole carriers' quantum confinement causes the wavelength of maximum exciton absorption (λ_{max}) to decrease as particle size decreases. NiO nanoparticles with and

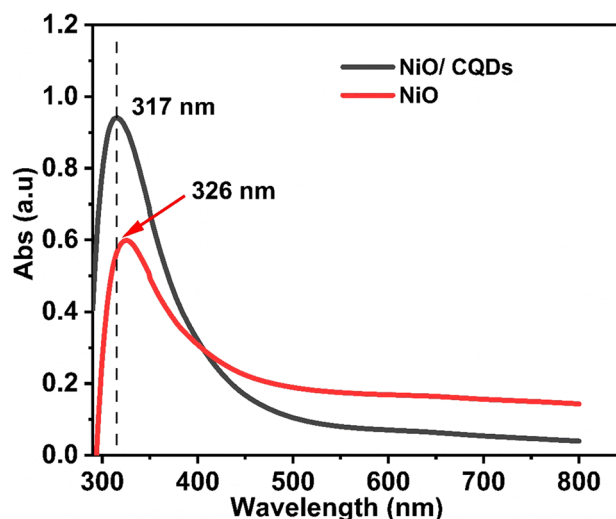


Fig. 6 Optical absorption for a thin film of NiO and NiO//QDs

without QDs show a blue shift in the absorption onset. A blue shift is seen, and the NiO nanoparticles with and without QDs absorption edge are found at 317 nm and 326 nm, respectively. The confinement of charge carriers within the nanoparticles is the primary cause of the blue shift observed in the absorption spectrum. The absorption peak of the NiO NPs without QDs is redshifted in absorption spectra compared to that of the NiO NPs with QDs. This wavelength redshift indicates that the band gap energy value of the NiO NP without QDs will decrease relative to the NiO NP with QDs. As the percentage of nanofiller weight increases compared to pure NiO, the absorbance of nanocomposites increases as well. This phenomenon suggests that the integration and interaction of NiO nanoparticles with QDs was successful. Moreover, the visible region of the nanocomposites' absorption spectra showed no peak. This result suggests that synthetic nanocomposite can be applied as a UV shielding and filtering block.

For high photon energies (h), the absorption coefficient is described as [46]:

$$\alpha = \frac{A(h\nu - E_g)^{1/2}}{h\nu} \quad (2)$$

E_g , α and A are the band gap, absorption coefficient, and constant, respectively. By extrapolating the linear region in the plots of $\frac{h\nu}{2}$ against $h\nu$, one can ascertain the nature of the optical band gap by utilizing the fundamental absorption corresponding to the optical transition of the electrons from the valence band to the conduction band. The optical band gap of the nanocrystalline NiO films was calculated from the UV–Vis to be 3.6 eV.

Applying the same procedure as in Sect. 3.1, the surface resistance of the bare NiO thin film, as well as that with QDs, is investigated in Fig. 7. A similar observation related to the reduction in the surface resistance

after adding QDs to the bare NiO is detected. However, another observation concerning the relatively higher surface resistance of the NiO, when compared to porous TiO₂, is recorded. We attribute such observation to the fact that porous TiO₂ exhibits a high surface area and interconnected pore network, enabling efficient charge transport and collection. The porous structure allows for a larger active surface area, promoting enhanced charge carrier mobility and reducing resistive losses.

In contrast, NiO typically has a lower surface area and a denser structure, leading to higher surface resistance due to limited charge transport pathways and increased resistive effects. Additionally, the electronic band structure and conductivity of TiO₂ are favorable for charge transport, further contributing to its lower surface resistance compared to NiO. Herein, the impact of adding QDs showed more significantly enhanced conductivity for the NiO thin films, with a 75% reduction in sheet resistance, while referring to TiO₂, cf—fig. 2, with only a 65% reduction.

3.3 CsPbCl₃ thin film characteristics

To examine the piezochemical properties of CsPbCl₃ with and without QDs, SEM, XRD, and FTIR characterization were conducted in Sect. 3.2. SEM analysis was performed and analyzed to observe the synthesized sample nanoparticles' morphological changes and surface morphological composition. The samples comprised uniformly sized CsPbCl₃ clusters that increased when QDs were added. Adding the QDs results in a large-scale accumulation of bounded proximal clustering (see Fig. 8). The image clearly shows how naturally highly agglomerated the particles were. When smaller particles aggregate or overlap, larger particles can result. Even at smaller sizes, the SEM images clearly show that the particles are randomly distributed and have a uniformly spherical shape.

Fig. 7 Morphological surface resistance for a thin film of **a** NiO and **b** NiO//QDs

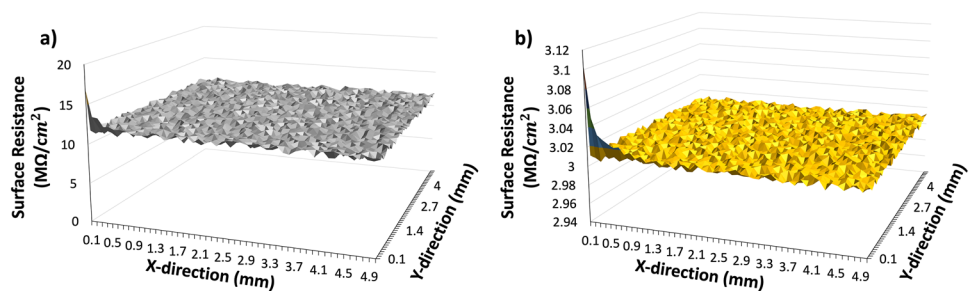


Fig. 8 SEM for a thin film of **a, c** CsPbCl₃, **b**, and **d** CsPbCl₃//QDs

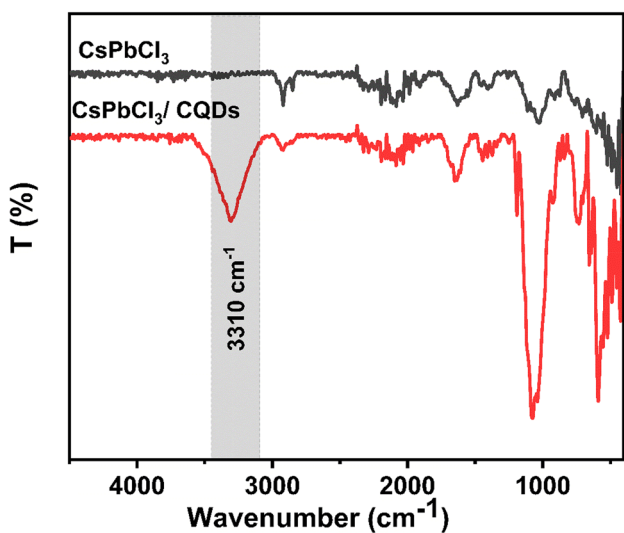
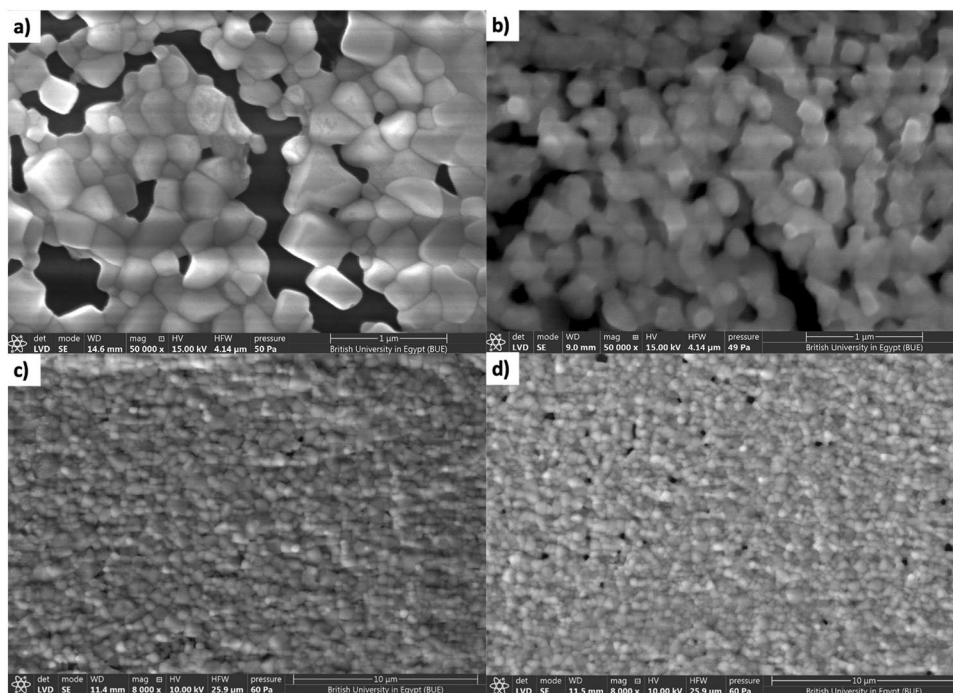


Fig. 9 FTIR for a thin film of CsPbCl₃ and CsPbCl₃//QDs

CsPbCl₃ nanoparticles appeared as tiny white particles and were uniformly distributed across the QD matrix's surface. As the amount of nanofiller in the nanocomposites increases, so does the inertia of the nanofillers to form agglomerations, leading to the formation of nanoclusters. The attractive van der Waals force causes nanoparticles to cluster between neighboring particles.

The FTIR spectra of CsPbCl₃ with and without QDs nanoparticles are displayed in Fig. 9, showing multiple

prominent absorption peaks. It shows the recorded FTIR spectrum from 4000 to 400 cm⁻¹. The absorption band's broadness suggests that the CsPbCl₃ powders are nanocrystals. The absorption peaks in FTIR spectra indicate a material's positions and chemical composition. The morphology, crystalline nature, and absorption peaks below 1000 cm⁻¹ are crucial for examining the presence of the bonds in CsPbCl₃ nanoparticles.

The absorbance bands, located at approximately 850–1250 cm⁻¹ and 1900–2400 cm⁻¹, respectively, reveal stretching vibrations of =CH and C=O and bending vibrations of -C=H. The C-H bending vibration originating from the methylene group was correlated with peaks at 1420 cm⁻¹. The C-H stretch vibrations are associated with peaks in the FTIR extract, which are situated between 2930 and 2852 cm⁻¹. A new broad band at 3100–3700 cm⁻¹ after QDs were doped with CsPbCl₃. This broadband was linked to the bending mode of H₂O molecules, the spinel structure of N-H, and the hydrogen vibration O-H. It is a sign of the stretching vibration mode of the chemically bonded hydroxyl group, usually associated with carboxylic acids and phenols. It is attributed to water absorbed on the outside surface of the sample. The intensity of these bands was found to increase following the addition of QDs during the calcination process, suggesting that the ultrafine powders did not have a strong tendency to absorb H₂O and CO₂. The presence of QDs

and CsPbCl₃ nanoparticles in the synthesized nanocomposites was detected by FTIR analysis, suggesting that their complexation was successful.

The perovskite structure was investigated using X-ray diffraction, and the discovered patterns are displayed in Fig. 10. The XRD patterns of CsPbCl₃ with and without QDs following calcination are displayed in Fig. 10. The hydroxide precursor's peaks appear broad, suggesting that the hydroxide's crystallites may be in the nanoscale range. They differ in crystal symmetry, crystallinity, and crystallite shape, all related to the variation in peak broadening. Sharpened reflection peaks were visible in the XRD patterns of the calcined sample, indicating an increase in the size of the CsPbCl₃ crystallites. The crystal planes of the CsPbCl₃ can be easily identified as (003), (100), (222), (110), (111), (201), (101), (200), (020), (211), (012), (022), (220), (300), and (222) based on the peaks positions that appear at $2\theta = 11^\circ, 15.88^\circ, 20^\circ, 22.45^\circ, 24.1^\circ, 25^\circ, 26.3^\circ, 30.8^\circ, 32.10^\circ, 33^\circ, 35^\circ, 35.9^\circ, 38^\circ, 39.48^\circ, 43^\circ, 45.86^\circ, 49^\circ, \text{ and } 51.70^\circ$, respectively. No impurity peaks were detected, and a pure cubic CsPbCl₃ peak was easily indexed with $a = b = c = 4.197 \text{ \AA}$. The obtained XRD patterns and those documented in the literature agree very well. Additionally, the high crystallinity of the synthesized nanoparticles confirms the large and sharp spread peaks, with the most substantial peak located in the (200) plane. The diffraction peaks of the generated CsPbCl₃ nanoparticles were very similar to those of the cubic crystalline structure,

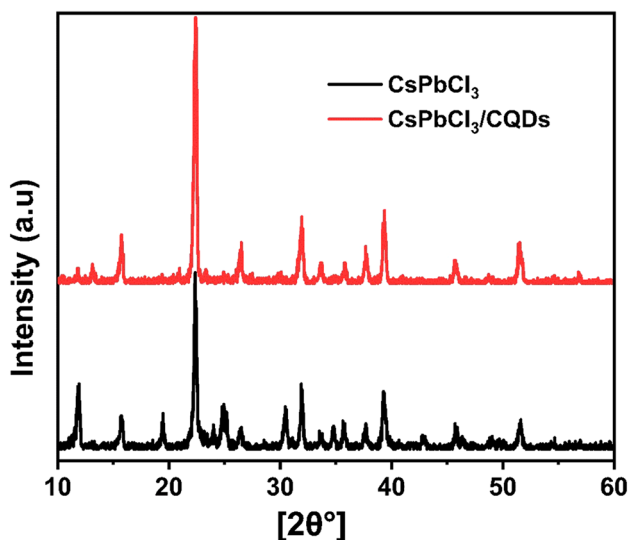


Fig. 10 XRD for a thin film of CsPbCl₃ and CsPbCl₃/QDs

suggesting that the samples are polycrystalline based on the presence of multiple peaks and their positions. Moreover, the XRD patterns of the sample showed no additional impure diffraction peaks.

As for the CsPbCl₃ NPs with QDs, the sample displayed a crystalline pattern, and all the diffraction peaks at approximately $2\theta = 11^\circ, 12^\circ, 15.88^\circ, 22.45^\circ, 26.3^\circ, 32.10^\circ, 33^\circ, 35^\circ, 35.9^\circ, 39.48^\circ, 46^\circ, 49^\circ, \text{ and } 52^\circ$ can be well indexed as face-centered cubic phases, which can be ideally related to the (003), (020), (100), (110), (101), (020), (130), (111), (012), (220), (131), (311), (222), (231,241), (200), (130), (300), and (222) crystal planes, respectively, based on the standard CsPbCl₃ pattern. When comparing nanosized CsPbCl₃ to CsPbCl₃/QDs, the (200) reflection is more intense, suggesting that the {100} family of planes in the nanostructured material contributes more to the overall pattern. Since the surface in this instance is nonpolar, Coulombic forces within the surface layer are effectively balanced, making the {100} orientation preferred at both CsPbCl₃ size regimes. The terminating surface contributes proportionately more to the diffraction pattern because it represents a more significant fraction of the nanoparticle material. This leads to an enhancement in the (200) diffraction feature.

Utilizing a UV–Visible spectrophotometer to examine the characterized optical absorption of the synthesized nanomaterials CsPbCl₃ and CsPbCl₃/QDs is demonstrated in Fig. 11a. The materials mentioned exhibit active optical absorption in the visible spectrum. However, the graphical representation makes it clear that there is an increase in the absorbance peak at the same wavelength of 410 nm when the CsPbCl₃ is doped with QDs. Herein, the Tauc plot method is utilized to estimate the bandgap of CsPbCl₃ and CsPbCl₃/QDs from the absorption spectra in Fig. 11a. By plotting $(h\nu)^2$ against $h\nu$ and identifying the linear region corresponding to band-to-band transitions, the bandgap energy can be estimated by extrapolating the linear portion to the X-axis, see Fig. 11b. This intersection provides an approximation of the bandgap energy, allowing for a straightforward determination of the material's bandgap using the absorption spectrum. The material's band gap is also adjusted to 1.5 eV with doping, cf. Figure 11b. As a result, photovoltaic solar cell applications can use these materials with adjustable band gaps.

The surface resistance is scanned for the bare sample and the QD-added sample in Fig. 12. Still, as in Sects. 3.2 and 3.3, the QDs sample epinastically

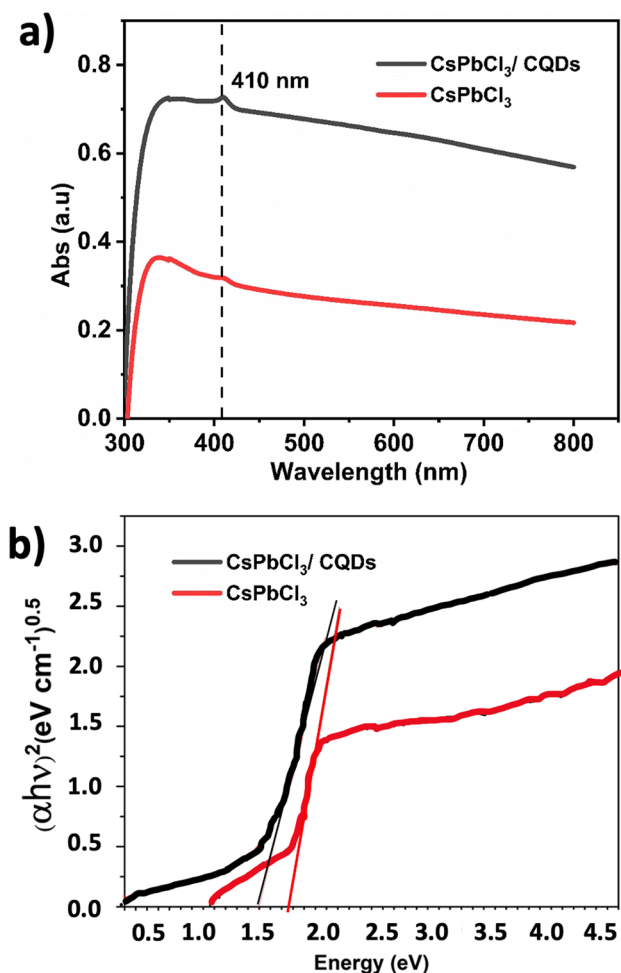


Fig. 11 **a** Optical absorption for a thin film of CsPbCl₃ and CsPbCl₃/QDs, and **b** Tauc plot showing $(h)^2$ against h

enhances the carrier mobility by a factor of 5.5. An ultra-huge surface resistance in sub-giga ohms is recorded for the bare perovskite sample. The high surface resistance of CsPbCl₃ thin films can be attributed to several factors. CsPbCl₃ is known for its intrinsic

insulating properties and wide bandgap, which hinder the mobility of charge carriers across the material’s surface.

Additionally, the crystal structure and surface morphology of CsPbCl₃ thin films can contribute to increased surface resistance, as the formation of grain boundaries and defects can impede charge transport. Furthermore, the ionic nature of CsPbCl₃ can lead to limited electronic conductivity, resulting in higher surface resistance. These combined factors contribute to the high surface resistance of CsPbCl₃ thin films, impacting their electrical properties and potential applications in optoelectronic devices.

Adding quantum to the perovskite material effectively reduces surface resistance through several mechanisms. Firstly, QDs serve as efficient charge carriers, facilitating the transport of electrons or holes within the material. This enhanced charge transport can mitigate resistive losses and improve overall conductivity, thereby reducing surface resistance. Additionally, the introduction of QDs modifies the material’s surface morphology and crystalline structure, promoting the formation of a more interconnected and conductive network; this is well observed in Fig. 12b resistance morphology against Fig. 12a. Moreover, carbon QDs, with suitable energy levels, act as additional electron or hole transport bridges, enabling effective charge transfer and reducing the impact of potential barriers, which contributes to lower surface resistance.

3.4 PSC I – V characteristics

Scaling up from the segmented solar cell, thin films, into a complete device is demonstrated in this section through eight different topologies, as in Fig. 1. The I – V characteristic curves for the eight architectures are presented in Fig. 13, where all macroscopic device parameters are listed in Table 2. Starting from the first

Fig. 12 Morphoacil surface resistance for a thin film of **a** CsPbCl₃ and **b** CsPbCl₃/QDs

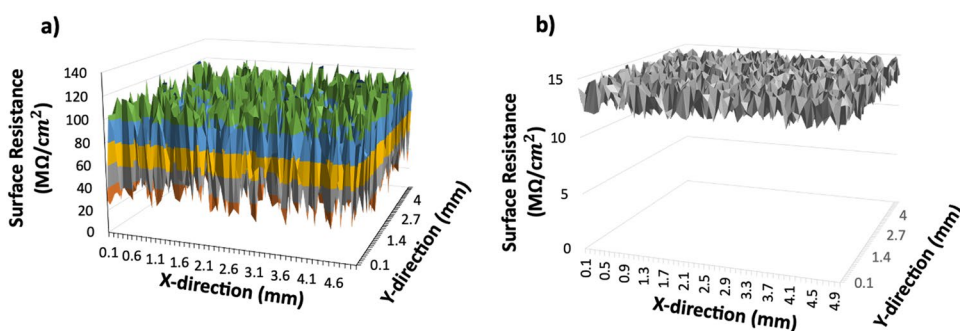


Fig. 13 The $I - V$ characteristics for **a** bare cesium lead chloride perovskite solar cells, while forward and backward light hysteresis curve, **b** Enhanced PSC structures from 1 to 3, **c** Enhanced PSC structures from 4 to 6, and **d** Enhanced PSC structures 7, while forward and backward light hysteresis curve

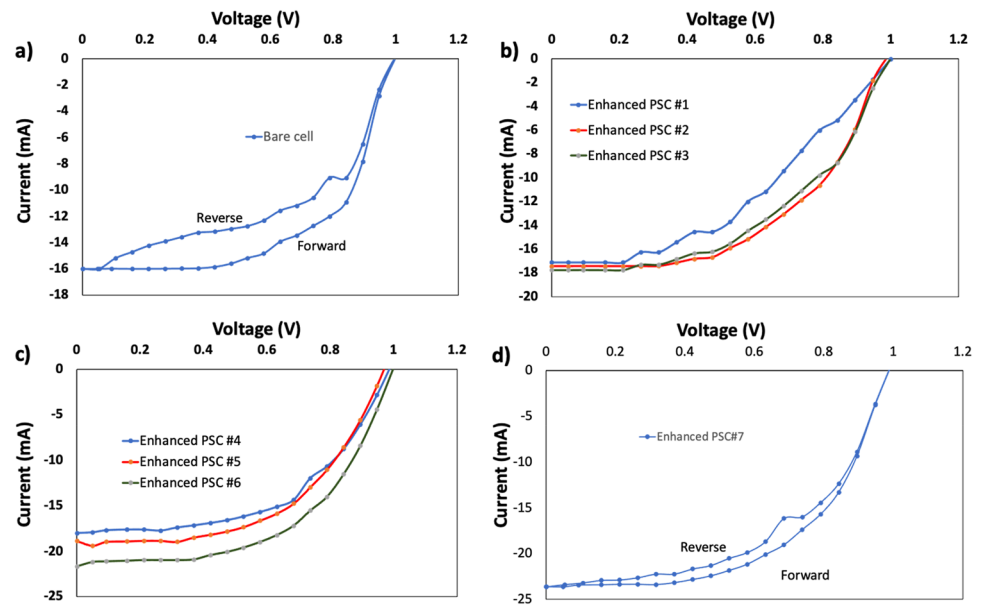


Table 2 extracted experimental parameters for the eight different PSCs investigated in this study with an active area of 25.5 mm^2

	V_{OC} (V)	I_{SC} (mA)	Error bar (%)	V_{mp} (V)	I_{mp} (mA)	FF	η (%)	Hysteresis index (%)
Bare Cell	0.98	16.0	4.8%	0.63	10.4	0.42	11.3	17.1
PSC #1	1.00	17.1	4.2%	0.52	13.7	0.42	12.3	23.2
PSC #2	0.99	17.4	4.1%	0.68	13.1	0.52	15.3	14.7
PSC #3	0.97	17.7	3.9%	0.63	13.5	0.49	14.7	13.2
PSC #4	0.98	18.0	3.7%	15.11	0.6	0.54	16.4	15.5
PSC #5	0.97	18.9	4.6%	14.77	0.7	0.55	17.4	11.2
PSC #6	0.97	21.7	4.2%	17.18	0.7	0.56	20.2	10.8
PSC #7	0.99	23.6	3.2%	19.09	0.7	0.56	22.5	6.8

set of curves in Fig. 13a, with a single layer QD in HTL, ETL, and perovskite layer, respectively. The hysteresis curves from the bare cell, and enhanced cell # 7 are plotted in Fig. 13a, and d, respectively, as forward and backward light measurements. Generally, the three integration models in topologies #1, #2, and #3 achieve better power conversion efficiency (PCE) concerning the bare sample. In the HTL, and based on the discussion in Sect. 3.2, the addition of the carbon-based QDs enhances the hole mobility, which contributes to the short-circuit current, as in Table 2. However, the impact of integrating the QDs in mp-TiO₂ recorded a better improvement in the PCS against the NiO/QD sample. This is well addressed when comparing the carrier transport capabilities in Fig. 2 with those in Fig. 7. Alternatively, embedding QDs in the perovskite layer introduces the highest short-circuit current among these three alternatives.

A trade-off between increasing the short-circuit current and the overall PCE is observed between PSC #2 and #3. Although the photon capturing associated with sample #2 is maximized, the hysteresis is also maximized, negatively impacting the PCE against sample #3, with minimum hysteresis among the first three sample sets. Adding quantum dots to the ETL layer in perovskite solar cells helps reduce hysteresis through several mechanisms. Hysteresis in perovskite solar cells is often attributed to ion migration and charge trapping at the interfaces and within the perovskite layer. When QDs are incorporated into the TiO₂ layer, they act as passivation agents and charge recombination centers, mitigating ion migration and reducing charge-trapping effects. This can lead to improved charge extraction and reduced recombination, ultimately minimizing hysteresis.

Additionally, the QDs modify the energy landscape and charge transport properties at the TiO₂/perovskite interface, promoting more efficient charge extraction and reducing the impact of hysteresis. Furthermore, the QDs can enhance the overall stability and performance of the perovskite layer, contributing to a more stable and reproducible device response, which can also help reduce hysteresis effects in perovskite solar cells. This is kept for further investigation as a future extension for this study.

Moving to the second set of samples, PSC #4, #5, and #6, where two QD layers are introduced. Combining efforts from the first set showed nearly the same expected trend. Adding the QDs in both ETL and the absorber reflects the top enhancement, reflecting the integration between maximum absorption and acceptable hysteresis. Finally, 22.5% PCE is reached for a triple-enhanced cell. In this structure, PSC #7, we sum up the potential of the QDs in PSC technology in one cell by adding quantum dots to the HTL, ETL, and the perovskite layer in a perovskite solar cell. QDs in the HTL act as charge transport and recombination centers, enhancing the charge extraction and reducing charge recombination at the HTL/perovskite interface. This led to improved charge collection and reduced losses, improving overall device efficiency. QDs in the ETL enhance electron transport and extraction, reducing electron trapping and improving charge collection at the ETL/perovskite interface. This improves electron extraction and reduces recombination, increasing device efficiency and stability. QDs in the perovskite layer modify the energy landscape, reduce charge trapping, and mitigate ion migration, leading to improved charge transport, reduced recombination, and enhanced stability. This results in improved device performance, reduced hysteresis, and enhanced operational stability, as a device forecasting, not discussed here. Overall, adding QDs to these layers leads to improved charge transport, reduced recombination, and enhanced stability, ultimately contributing to the improved performance and efficiency of perovskite solar cells.

4 Conclusion

In conclusion, integrating quantum dots (QDs) into various layers of perovskite solar cells (PSCs) has shown significant potential for improving device performance and efficiency. The addition of QDs in the

electron transport layer (ETL), hole transport layer (HTL), and perovskite absorber has enhanced charge transport, reduced recombination, and improved stability. This study has demonstrated that QDs can mitigate hysteresis effects in PSCs by reducing ion migration and charge trapping, ultimately leading to improved charge extraction and reduced recombination. The trade-off between short-circuit current and overall power conversion efficiency (PCE) with different QD integration strategies highlights the need for further optimization. The findings suggest that QDs can potentially enhance PSCs' operational stability and forecasting. Overall, the addition of QDs to various layers of PSCs holds promise for advancing the performance and efficiency of perovskite solar cell technology. Further research could develop more stable and efficient PSCs for practical applications.

Acknowledgements

The authors would like to acknowledge the support and contribution of The Centre of Emerging Learning Technologies (CELT), FabLab, and The Nanotechnology Research Centre (NTRC) at the British University in Egypt. Special thanks to Ms. Mona Samir, research assistant at NTRC, for her support in preparing NiO suspension.

Authors' contributions

All authors have contributed equally.

Funding

Open access funding provided by The Science, Technology & Innovation Funding Authority (STDF) in cooperation with The Egyptian Knowledge Bank (EKB).

Data availability

The data supporting this study's findings are available from the corresponding author upon reasonable request.

Code availability

Not applicable for that section.

Declarations

Conflict of interest The Authors declare that there is no conflict of interest.

Ethical approval Not applicable.

Consent to participant All authors confirm their participation in this paper.

Consent for publication All authors accept the publication rules applied by the journal.

Open Access This article is licensed under a Creative Commons Attribution 4.0 International License, which permits use, sharing, adaptation, distribution and reproduction in any medium or format, as long as you give appropriate credit to the original author(s) and the source, provide a link to the Creative Commons licence, and indicate if changes were made. The images or other third party material in this article are included in the article's Creative Commons licence, unless indicated otherwise in a credit line to the material. If material is not included in the article's Creative Commons licence and your intended use is not permitted by statutory regulation or exceeds the permitted use, you will need to obtain permission directly from the copyright holder. To view a copy of this licence, visit <http://creativecommons.org/licenses/by/4.0/>.

References

- Z.S. Ismail, E.F. Sawires, F.Z. Amer, S.O. Abdellatif, Experimentally verified analytical models for the dynamic response of perovskite solar cells using measured I–V and C–V characteristics. *Opt. Quant. Electron.* **55**(14), 1272 (2023). <https://doi.org/10.1007/s11082-023-05304-8>
- Z. Wu et al., Passivation strategies for enhancing device performance of perovskite solar cells. *Nano Energy* (2023). <https://doi.org/10.1016/j.nanoen.2023.108731>
- A. Mohammad, F. Mahjabeen, Promises and challenges of perovskite solar cells: a comprehensive review. *BULLET: Jurnal Multidisiplin Ilmu* **2**(5), 1147–1157 (2023)
- H. Zhang, L. Pfeifer, S.M. Zakeeruddin, J. Chu, M. Grätzel, Tailoring passivators for highly efficient and stable perovskite solar cells. *Nat. Rev. Chem.* **7**(9), 632–652 (2023)
- O. Al-Saban, M. Alkadi, S.M.H. Qaid, A.A.A. Ahmed, S.O. Abdellatif, Machine learning algorithms in photovoltaics: evaluating accuracy and computational cost across datasets of different generations, sizes, and complexities. *J. Electron. Mater.* (2024). <https://doi.org/10.1007/s11664-023-10897-7>
- W. Wu et al., Recent progress on wavelength-selective perovskite photodetectors for image sensing. *Small Methods* **7**(4), 2201499 (2023)
- J. Moon, Y. Mehta, K. Gundogdu, F. So, Q. Gu, Metal-halide perovskite lasers: cavity formation emission characteristics. *Adv. Mater.* (2023). <https://doi.org/10.1002/adma.202211284>
- A. Liu et al., High-performance metal halide perovskite transistors. *Nat. Electron.* **6**(8), 559–571 (2023)
- Y.-K. Wang et al., Self-assembled monolayer-based blue perovskite LEDs. *Sci. Adv.* **9**(36), eadh2140 (2023)
- M.M. Hassan, Z.S. Ismail, E.M. Hashem, R. Ghannam, S.O. Abdellatif, Investigating the tradeoff between transparency and efficiency in semitransparent bifacial mesostructured solar cells for millimeter-scale applications. *IEEE J. Photovolt.* **11**(5), 1222–1235 (2021)
- S.O. Abdellatif, A. Fathi, K. Abdullah, M.M. Hassan, Z. Khalifa, Investigating the variation in the optical properties of TiO₂ thin-film utilized in bifacial solar cells using machine learning algorithm. *J. Photonics Energy.* **12**(2), 022202–022202 (2022)
- T. Hatem, Z. Ismail, M.G. Elmahgary, R. Ghannam, M.A. Ahmed, S.O. Abdellatif, Optimization of organic mesostructured solar cells for underwater IoT 2 self-powered sensors. *IEEE Trans. Electron. Devices.* **68**(10), 5319–5321 (2021)
- A.M. Mahran, S.O. Abdellatif, Optoelectronic modelling and analysis of transparency against efficiency in perovskites/dye-based solar cells, in *2021 International Conference on Microelectronics (ICM)*, 2021: IEEE, pp. 178–181
- Z.S. Ismail, E.F. Sawires, F.Z. Amer, S.O. Abdellatif, Perovskites informatics: Studying the impact of thicknesses, doping, and defects on the perovskite solar cell efficiency using a machine learning algorithm, *Int. J. Numer. Model.: Electron. Networks, Devices Fields*
- M.M. Salah, Z. Ismail, S. Abdellatif, Selecting an appropriate machine-learning model for perovskite solar cell datasets. *Mater. Renew. Sustain. Energy* **12**(3), 187–198 (2023)

16. N. Li, X. Niu, Q. Chen, H. Zhou, Towards commercialization: the operational stability of perovskite solar cells. *Chem. Soc. Rev.* **49**(22), 8235–8286 (2020)
17. F. Wu et al., Effects of electron-and hole-current hysteresis on trap characterization in organo-inorganic halide perovskite. *J. Energy Chem.* **76**, 414–420 (2023)
18. J. Liu et al., Influence of hole transport layers/perovskite interfaces on the hysteresis behavior of inverted perovskite solar cells. *ACS Appl. Energy Mater.* **3**(7), 6391–6399 (2020)
19. M. Wang, Y. Lei, Y. Xu, L. Han, Z. Ci, Z. Jin, The J–V hysteresis behavior and solutions in perovskite solar cells. *Solar RRL* **4**(12), 2000586 (2020)
20. T. Zhang, Q. He, J. Yu, A. Chen, Z. Zhang, J. Pan, Recent progress in improving strategies of inorganic electron transport layers for perovskite solar cells. *Nano Energy* (2022). <https://doi.org/10.1016/j.nanoen.2022.107918>
21. Y. Li, Z. Li, F. Liu, J. Wei, Defects and passivation in perovskite solar cells. *Surf. Innov.* **10**(1), 3–20 (2022)
22. X. Gu, W. Xiang, Q. Tian, S. Liu, Rational surface-defect control via designed passivation for high-efficiency inorganic perovskite solar cells. *Angew. Chem. Int. Ed.* **60**(43), 23164–23170 (2021)
23. R. Montecucco, E. Quadrivi, R. Po, G. Grancini, All-inorganic cesium-based hybrid perovskites for efficient and stable solar cells and modules. *Adv. Energy Mater.* **11**(23), 2100672 (2021)
24. W. Xiang, S. Liu, W. Tress, Interfaces and interfacial layers in inorganic perovskite solar cells. *Angew. Chem.* **133**(51), 26644–26657 (2021)
25. A.S. Sadhu, Y.-M. Huang, L.-Y. Chen, H.-C. Kuo, C.-C. Lin, Recent advances in colloidal quantum dots or perovskite quantum dots as a luminescent downshifting layer embedded on solar cells. *Nanomaterials* **12**(6), 985 (2022)
26. F.P. García de Arquer, D.V. Talapin, V.I. Klimov, Y. Arakawa, M. Bayer, E.H. Sargent, Semiconductor quantum dots: technological progress and future challenges. *Science* **373**(6555), eaaz8541 (2021)
27. S.-J. Jeong et al., Zero dimensional–two dimensional hybrid photodetectors using multilayer MoS₂ and lead halide perovskite quantum dots with a tunable bandgap. *ACS Appl. Mater. Interfaces* **15**(4), 5432–5438 (2023)
28. H. Shabbir, M. Wojnicki, Recent progress of non-cadmium and organic quantum dots for optoelectronic applications with a focus on photodetector devices. *Electronics* **12**(6), 1327 (2023)
29. P. Rani, R. Dalal, S. Srivastava, Effect of surface modification on optical and electronic properties of graphene quantum dots. *Appl. Surf. Sci.* **609**, 155379 (2023)
30. W. Chi, S.K. Banerjee, Development of perovskite solar cells by incorporating quantum dots. *Chem. Eng. J.* **426**, 131588 (2021)
31. X. Li et al., Evidence for ferroelectricity of all-inorganic perovskite CsPbBr₃ quantum dots. *J. Am. Chem. Soc.* **142**(7), 3316–3320 (2020)
32. J. Yuan et al., Metal halide perovskites in quantum dot solar cells: progress and prospects. *Joule* **4**(6), 1160–1185 (2020)
33. S. Lim et al., Monodisperse perovskite colloidal quantum dots enable high-efficiency photovoltaics. *ACS Energy Lett.* **6**(6), 2229–2237 (2021)
34. H. Li et al., Self-assembly of perovskite CsPbBr₃ quantum dots driven by a photo-induced alkynyl homocoupling reaction. *Angew. Chem. Int. Ed.* **59**(39), 17207–17213 (2020)
35. Y. Bai, M. Hao, S. Ding, P. Chen, L. Wang, Surface chemistry engineering of perovskite quantum dots: strategies, applications, and perspectives. *Adv. Mater.* **34**(4), 2105958 (2022)
36. M. Hao, S. Ding, S. Gaznaghi, H. Cheng, L. Wang, Perovskite quantum dot solar cells: current status and future outlook: focus review. *ACS Energy Lett.* **9**, 308–322 (2024)
37. H. Shen et al., Thiosulfate-terminated CdSe quantum dots for improving the performance and stability of perovskite solar cells. *Mater. Today Chem.* **35**, 101831 (2024)
38. S. Abdellatif et al., Refractive index and scattering of porous TiO₂ films. *Microporous Mesoporous Mater.* **264**, 84–91 (2018). <https://doi.org/10.1016/j.micromeso.2018.01.011>
39. S.O. Abdellatif, S. Josten, A.S. Khalil, D. Erni, F. Marlow, Transparency and diffused light efficiency of dye-sensitized solar cells: tuning and a new figure of merit. *IEEE J. Photovolt.* **10**(2), 522–530 (2020)
40. T. Hatem, M.G. Elmahgary, R. Ghannam, M.A. Ahmed, S.O. Abdellatif, Boosting dye-sensitized solar cell efficiency using AgVO₃-doped TiO₂ active layer. *J. Mater. Sci.: Mater. Electron.* **32**, 25318–25326 (2021)
41. S. Abdellatif et al., Optical investigation of porous TiO₂ in mesostructured solar cells. *Phys. Simul. Optoelectron. Devices XXVI* **10526**, 38–46 (2018)
42. M. Samir, Z. Ismail, A.M. Agour, H. Nageh, S.O. Abdellatif, Exploring forward scattering mechanisms in TiO₂ with carbon quantum dots: insights into photovoltaic applications. *Opt. Mater.* (2024). <https://doi.org/10.1016/j.optmat.2024.114922>
43. M. Samir, A.M. Agour, Z. Ismail, H. Nageh, S.O. Abdellatif, The impact of N-doped carbon quantum dots on dye-sensitized solar cells operating under diffused- and low-light intensity. *IEEE J. Photovolt.* (2023). <https://doi.org/10.1109/JPHOTOV.2023.3336474>

44. K.I. Alabid, H.N. Nasser, Synthesis and characterization of nickel oxide with nitrogen quantum carbon dots as nanoadsorbent (NiO–NCQD) nanocomposite. *Int. J. Nano Dimens.* **14**(3), 227–237 (2023)
45. A.M. Al-Enizi, M. Ubaidullah, D. Kumar, Carbon quantum dots (CQDs)/Ce doped NiO nanocomposite for high performance supercapacitor. *Mater. Today Commun.* **27**, 102340 (2021)
46. M.G. Elmahgary, A.M. Mahran, M. Ganoub, S.O. Abdelatif, Optical investigation and computational modelling of

BaTiO₃ for optoelectronic devices applications. *Sci. Rep.* **13**(1), 4761 (2023)

Publisher's Note Springer nature remains neutral with regard to jurisdictional claims in published maps and institutional affiliations.